Title	Attachment of solid elongated particles on the surface of a stationary gas bubble
Author(s)	Lecrivain, Gregory; Petrucci, Giacomo; Rudolph, Martin; Hampel, Uwe; Yamamoto, Ryoichi
Citation	International Journal of Multiphase Flow (2015), 71: 83-93
Issue Date	2015-05
URL	http://hdl.handle.net/2433/196088
Right	2015 Elsevier Ltd. NOTICE: this is the author's version of a work that was accepted for publication in International Journal of Multiphase Flow. Changes resulting from the publishing process, such as peer review, editing, corrections, structural formatting, and other quality control mechanisms may not be reflected in this document. Changes may have been made to this work since it was submitted for publication. A definitive version was subsequently published in International Journal of Multiphase Flow, 71, 2015, doi:10.1016/j.ijmultiphaseflow.2015.01.002
Type	Journal Article
Textversion	author

Graphical Abstract (for review)

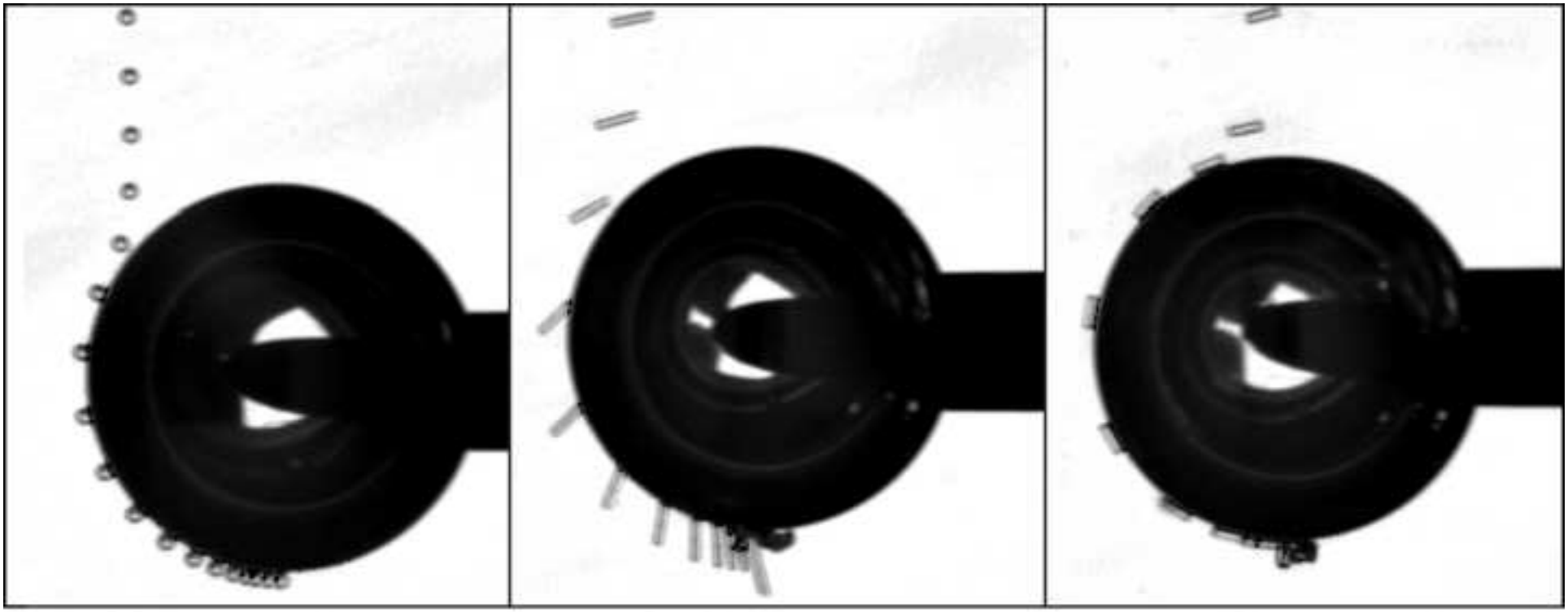

Sphere attachment *Weak fibre attachment* *Strong fibre attachment*

Highlights:

- Attachment of elongated particles on a gas bubble is investigated
- Translational particle velocities are compared with simulated data
- Two kinds of attachments, which depend on the collision area, are discovered
- Results are relevant to three-phase flow separation processes such as flotation

Attachment of solid elongated particles on the surface of a stationary gas bubble

Gregory Lecrivain[1,2,†], Giacomo Petrucci[2,3], Martin Rudolph[4], Uwe Hampel[2,5] and Ryoichi Yamamoto[1]

[1] Kyoto University,
Department of Chemical Engineering,
Kyoto 615-8510,
Japan.

[2] Helmholtz-Zentrum Dresden-Rossendorf,
Institute of Fluid Dynamics,
Bautzner Landstraße 400,
01328 Dresden,
Germany.

[3] Università di Modena e Reggio Emilia,
Dipartimento di Ingegneria "Enzo Ferrari",
Via Vignolese, 905/B,
41125 Modena,
Italy.

[4] Helmholtz-Zentrum Dresden-Rossendorf,
Helmholtz-Institute Freiberg for Resource Technology,
Halsbrücker Str. 34,
09599 Freiberg,
Germany.

[5] Technische Universität Dresden
Institut für Energietechnik
AREVA-Stiftungsprofessur für Bildgebende Messverfahren für die Energie- und Verfahrenstechnik,
01062 Dresden,
Germany.

[†]corresponding author:
Tel. : +81-(0)75-383-2651
Fax. : +81(0)75-383-2651
g.lecrivain@hzdr.de

Abstract:

Froth flotation is a separation process which plays a major role in the mining industry. It is essentially employed to recover a vast array of different valuable commodities such as rare earth minerals essential to the manufacture of high-tech products. Owing to its simplicity, the process is also widely used for de-inking recycled paper fibres and for waste water treatment. The flotation process essentially relies on the attachment of solid particles on the surface gas bubbles immersed in water. The present study seeks to investigate the effect of the particle shape on the attachment mechanism. Using an in-house optical micro-bubble sensor the approach, the sliding and the adhesion of micron milled glass fibres on the surface of a stationary air bubble immersed in stagnant water is thoroughly investigated. The translational and rotational velocities were measured for fibres of various aspect ratios. The results are compared with a theoretical model and with experimental data obtained with spherical glass beads. It is found that the fibre orientation during the sliding motion largely depends on the collision area. Upon collision near the upstream pole of the gas bubble the major axis of the fibre aligns with the local bubble surface (tangential fibre alignment). If collision occurs at least 30° further downstream only head of the fibre is in contact with the gas-liquid interface (radial fibre alignment).

Keywords: Froth flotation, three-phase system, solid elongated particles, particle attachment, gas-liquid interface.

1. Introduction

1.1. Motivation

Froth flotation is a versatile separation process which plays a major role in the mining industry. It is essentially employed to recover a vast array of different valuable commodities such as copper, zinc, nickel, phosphate and rare earth minerals essential to the manufacture of high-tech products (Fuerstenau, Jameson *et al.*, 2007). Owing to its simplicity, the process has more recently seen widespread applications in the non-mining field. Flotation is for instance used for the de-inking of recycled paper fibres (Kemper, 1999) and for the removal of pollutants from waste water (Rubio, Souza *et al.*, 2002). In mineral froth flotation the separation can be accomplished in a flotation cell, which is essentially a tank fitted with an impeller (Ahmed and Jameson, 1985). The impeller disperses air into fine gas bubbles and agitates the slurry. It provides a favourable environment in the cell for the promotion of bubble collision with the finely ground ore (Fuerstenau, Jameson *et al.*, 2007). Typical values of particle diameters, for which the recovery rate is high, vary from approximately $d_p = 10$ µm to $d_p = 150$ µm (Tao, 2005, Jameson, 2010). Many ore minerals are naturally hydrophilic. The addition of so-called "collectors" to the slurry, which are absorbed by the mineral surface, renders the precious mineral particles hydrophobic (Rosenqvist, 2004). The hydrophobised particles then attach to the surface of the rising bubbles, whose size generally ranges from $d_b = 0.6$ to 2 mm in diameter (Rubio, Souza *et al.*, 2002). The particle-bubble aggregates are conveyed to the top of the flotation cell to form a rich mineral-laden froth layer, which eventually overflows into a launder as a separate product. Since pure liquids generally do not foam, "frothers" are utilised to control the bubble size and to stabilise the froth (Cho and Laskowski, 2002). The gangue, i.e. the commercially valueless hydrophilic material, eventually exits the flotation cell as slurry.

1.2. Particle shape

Ore grinding in froth flotation is an important step to liberate the valuable mineral particles from the gangue (Forssberg, Subrahmanyam *et al.*, 1993). Kursun and Ulusoy (2006) showed for instance that the shape of talc mineral particles produced by milling considerably deviated from an ideal sphere. Talc minerals ground by rod milling showed higher elongation and flatness than those ground by ball milling. The study of Rahimi, Dehghani *et al.* (2012) also suggested that rod milling caused an elongation of the particles and that ball milling caused a greater particle roundness. Various studies have shown that the particle elongation increases the recovery rate.

Koh, Hao *et al.* (2009) found that ground ballotini particles had a higher recovery rate than spherical ballotini particles. The work of Yekeler, Ulusoy *et al.* (2004) also corroborated this finding. The team experimentally observed that particle elongation increased the ease, with which a particle attaches to a bubbles surface. Particle roundness tended to have an adverse effect on the recovery rate. Note, that the recovery rate k is the rate at which the desired particles are recovered from the suspension. In a flotation tank, the number concentration $c(t)$ of the desired particles will decay exponentially with time. Ahmed and Jameson (1985) suggested the following formula $c(t) = c_0 \exp(-kt)$, where c_0 was the initial concentration in the tank.

1.3. Particle attachment on bubble surface

The attachment of a solid particle on the surface of a gas bubble can be divided into three successive stages: the particle approach, the collision with the bubble and the sliding down the gas-bubble interface (Schulze, 1989, Albijanic, Ozdemir *et al.*, 2010). The downward sliding motion of the particle is caused by the gravity and also by the hydrodynamic forces arising from the local water flow around the rising bubble. Should the particle approach the bubble surface within the range of attractive surface forces, a thin intervening liquid film between the gas-liquid interface and the solid-liquid interface forms. The liquid film eventually drains, leading to a critical thickness at which rupture occurs (Ralston, Fornasiero *et al.*, 1999). The rupture of the liquid film results in the formation of a stable three-phase contact (Schulze, 1992). The deployment of high speed camera systems has been favoured in recent years to observe the particle attachment in great detail. Wang, Zhou *et al.* (2003a) photographically recorded the attachment of free falling spherical glass beads on a stationary air bubble, which had undergone various surface treatments. Gu, Sean Sanders *et al.* (2004) investigated the attachment of rising spherical hydrogen bubbles on a larger fixed bitumen particle. Hubička, Basařová *et al.* (2013) measured the trajectories of an approaching large solid spherical particle on a stationary gas bubble. The sliding was however left out by the authors. Verrelli, Bruckard *et al.* (2014) were the first to look at the attachment of non-spherical particles. They measured the induction time, i.e. the time required for the liquid film to thin to its critical film thickness (Ye, Khandrika *et al.*, 1989), of 'angular frit' particles falling on a gas bubble. The above state of the art clearly shows that the attachment process has largely been limited to the attachment of perfectly spherical particles. The effect of shape irregularity on the attachment process has received scarce attention. To date only one attempt can be found in the literature. The present piece of work aims to

alleviate this shortcoming by experimentally investigating the attachment of elongated particles with an aspect ratio of up to 7.

2. Methods

2.1. Experimental facility

The experimental procedure employed to visualise attachment of solid particles was inspired by the work of Verrelli, Bruckard *et al.* (2014). As illustrated in Figure 1 the experimental set-up essentially consisted of water tank in which a needle was placed in a horizontal position. The 25 gauge ultra-smooth hydrophobic needle with a ta-C diamond-like carbon coating (SGE Analytical Science, Diamond MS Syringe 0355321) was attached to a 50 µl precision syringe (Hamilton, 1805RNSYR). It allowed blowing a stable and stationary air bubble, whose diameter could be varied from $d_b = 1.3$ mm to $d_b = 1.7$ mm. A larger bubble diameter resulted in a detachment of the gas bubble from the needle. The adhesion force holding the bubble on the needle tip could no longer overcome the buoyancy force. The present bubble size range matched the typical size range frequently found in other literature data (Huang, Legendre *et al.*, 2011). The water was kept at a constant room temperature of 20 ˚C and had a pH value of 7.8. The opened-water tank was made of transparent Plexiglas walls. A tube fastened in a vertical position had its immersed extremity placed 15 mm away from the bubble upper pole (henceforth referred to as the upstream pole), which corresponded to a distance of about 10 bubble diameters. The reason behind the use of the fastened vertical tube was threefold: 1. to guide the particles all the way down to the gas bubble, 2. to avoid an interference of the falling particle with the surrounding liquid and 3. to hold the Pasteur pipette in a stable vertical position. The Pasteur pipette, containing the particles heavily diluted in water, could then be placed in the tube in question. The bulb of the pipette in contact with ambient air was pierced to avoid a squeezing that would potentially give the particles an undesired acceleration. By releasing the finger from the bulb the solid particles could start their decent with an initial velocity close to zero. The present facility unfortunately did not exactly reproduce all mechanisms observed in an industrial flotation cell. The motion of the liquid and of the gas phases were here left out, and so were the effect of frother and collector addition. To the best of the authors' knowledge the present study, even though it is a fairly simple system, is the first of its kind that seeks to investigate the effect of particle elongation on the overall attachment mechanism, which is of chief importance in the flotation process. It is hoped that the present results will help build more complex models in the future.

2.2. Solid particles

Experimental tests were performed with spherical particles for comparison purposes and fibre-like elongated particles. The glass spherical particles (Wiwox, STGP002) had a particle-to-liquid density ratio of $S = \rho_S / \rho_L = 2.45$ and a diameter ranging from $d_p = 50$ µm to $d_p = 100$ µm. The milled glass fibres (3B-Fibreglass, MF01ER) had a particle-to-liquid density ratio of $S = 2.5$ and a length ranging from 100 µm to 200 µm in the long-axis direction (major axis). Detailed images of the elongated particles obtained from the on-site Scanning Electron Microscope which operates under high vacuum conditions (Zeiss EVO 50) revealed an aspect ratio, defined as the ratio of fibre length to diameter, ranging from $e = 1$ to $e = 7$. Figure 2a illustrates high-resolution images of spherical particles. The small structures on the surface of the elongated particles (Figures 2b) are probably smaller glass particles. This highly polydispersity in the particle size distribution can be seen in Figure 2c.

A spherical particle falling in stagnant water eventually reaches its terminal velocity

$$u_\infty = g\left(\frac{Sd_p^2}{18\nu}\right)\left(1 - \frac{1}{S}\right) = g\tau\left(1 - \frac{1}{S}\right), \quad (1)$$

where g is the gravity and $\nu = \mu/\rho_L$ is the liquid kinematic viscosity, i.e. the ratio of the liquid dynamic viscosity to the liquid density. The terminal velocity of a spherical particle can be conveniently expressed using the particle response time τ. This time corresponds to the time required by a particle to respond to a change in the liquid velocity (Crowe, Schwarzkopf *et al.*, 2011). The response time τ is defined as

$$\tau = \frac{Sd_p^2}{18\nu}. \quad (2)$$

For an elongated particle the terminal velocity will be affected by the orientation of the major axis relative to direction of motion. In the present work the direction of motion simply coincides with the direction of the gravity g since the liquid is at rest. The terminal velocity of an elongated particle with an aspect ratio of $e = 6$ will differ by up to 60% to that of a spherical particle with equivalent volume (Kasper, Niida *et al.*, 1985). Further analysis on the terminal velocity of an elongated particle is dealt with in greater detail in the discussion section.

2.3. Particle hydrophobicity

The determination of the particle hydrophobicity is not straightforward and often requires special instrumentation. The sessile method, one of the simplest available methods, which involves the optical measurement of the contact angle of a droplet at rest on a substrate, will often fail for powder (Susana, Campaci *et al.*, 2012). In addition the sole determination of the contact angle between a solid surface and a gas-liquid interface does not allow for the exact description of the surface hydrophobicity since specific and aspecific interactions need to be considered. Consequently, two surfaces with the same contact angle with water can actually have a different hydrophobicity (van Oss, 2003). To overcome this, inverse gas chromatography (Mohammadi-Jam and Waters, 2014) was presently used to measure the specific surface free energies of the two sets of powder previously described in section 2.2. The inverse gas chromatography measurement device (Surface Energy Analyser, Surface Measurement Systems) was here used for determination of the disperse component γ^d, the Lewis acid component $\gamma^+$and the Lewis base component γ^- of the specific surface free energy at surface coverages of 1 %, of 20 % and of an extrapolation to 100 % (Das, Larson *et al.*, 2011, Gamble, Leane *et al.*, 2012). The variation in the percentage of the surface coverage allowed an assessment of the heterogeneity in the surface energy. The total surface free energy was then calculated as follows

$$\gamma^t = \gamma^d + 2\sqrt{\gamma^+\gamma^-}. \quad (3)$$

Prior to the determination of the surface free energy at different surface coverages, the specific surface area of the two sets of particles per unit mass S_m^{BET} were determined with the N_2-BET method (Brunauer, Emmett *et al.*, 1938) using special instrumentation (FlowSorb II 2300, Micromeritics). The specific surface area per unit mass helped determine the amount of probe gases needed for a given surface coverage. For the determination of the disperse component heptane, octane, nonane and decane probe gas molecules were carried by a helium gas flowing at a rate of 10 cm^3/min. Monopolar ethyl acetate was used for the determination of the Lewis acid component and dichloromethane for the Lewis base, respectively. The column was operated at 0 % humidity and at a 90°C temperature to ensure a clean surface, which in-turn guaranteed a desorption throughout the entire measurement procedure. A mass sample was chosen so that the surface area equalled 0.5 m^2. The samples were tapped vertically for ten minutes in a 3-mm inner diameter and 30-cm length column, which was sealed with inert silanized glass wool. Prior to the measurement the samples were conditioned at a 100°C temperature for a period of 5 hours in a

helium gas also flowing at 10 cm^3/min. The specific surface free energy components were calculated using the peak maximum of the probe molecule retention. The Schultz approach was employed for the disperse component γ^d, the van Oss-Chaudhury-Good/Della-Volpe approach for the Lewis acid/basic component (Das, Larson *et al.*, 2011). To thermodynamically evaluate whether the particle attachment to a gas bubble is actually favourable in liquid water the specific free energy of interaction ΔG_{pwb} was calculated as follows (van Oss, 2003)

$$\Delta G_{pwb} = \left(\sqrt{\gamma_S^d} - \sqrt{\gamma_G^d}\right)^2 - \left(\sqrt{\gamma_S^d} - \sqrt{\gamma_L^d}\right)^2 - \left(\sqrt{\gamma_G^d} - \sqrt{\gamma_L^d}\right)^2 + 2\left(\sqrt{\gamma_L^+}\left[\sqrt{\gamma_S^-} + \sqrt{\gamma_G^-} - \sqrt{\gamma_L^-}\right] + \sqrt{\gamma_L^-}\left[\sqrt{\gamma_S^+} + \sqrt{\gamma_G^+} - \sqrt{\gamma_L^+}\right] - \sqrt{\gamma_S^+\gamma_G^-} - \sqrt{\gamma_p^-\gamma_G^+}\right). \quad (4)$$

The subscript L, G and S respectively denote the specific free surface energies of the liquid water (L), of the gas bubble (G) and of the solid particles (S). Finally the contact angle θ between the particle surface and the liquid water was determined using the surface free energy components as follows (van Oss, 2003)

$$\theta = \cos^{-1}\left(\frac{2}{\gamma_L^t}\cdot\left[\sqrt{\gamma_S^d\gamma_L^d} + \sqrt{\gamma_S^+\gamma_L^-} + \sqrt{\gamma_S^-\gamma_L^+}\right] - 1\right). \quad (5)$$

The results are summarised in Table 1. The three components of the total specific energy for the air bubble and for the liquid water were taken from the literature (van Oss, Giese *et al.*, 2005, VDI-GVC, 2013). Findings from the present inverse gas chromatography measurements show that, for the two sets of particles and under all surface coverages, the specific free energy ΔG_{pwb} is always negative and thus attachment is favourable in all cases. Thermodynamically speaking, the particles are indeed hydrophobic. Irrespective of the surface coverage, the specific free energy ΔG_{pwb} shows little heterogeneity for the spherical particles and the values of the free specific interactions and of the contact angles are all similar. The same cannot be said for the elongated particles. At a surface coverage of the 1% there is a higher polarity for the elongated particles, which resulted in smaller contact angles and a lower free energy of interactions with a bubble in water. Compared to the spherical particles the hydrophobicity at 10 % and at 100 % coverage is greater. It is expected from the present results that the elongated particles will attach to the gas bubble slightly differently. The study also revealed a contact angle lying in the range $60° < \theta < 70°$. Fuerstenau, Jameson *et al.* (2007) showed that this contact angle is large enough to achieve a good floatability in the flotation process. The present contact angle slightly overestimates the values worked out by Tino, Dieter *et al.* (1996) and by Nowak, Robbins *et al.* (2013) who reported contact angles ranging from 50° to 60°. The calculation of their contact angles was

performed using the sessile method, which involved a water droplet was at rest on a glass substrate. Last but not least, even with a surface treatment involving for instance chlorotrimethylsilane, the contact angle of smooth spherical glass beads can only be increased to about 90° (Nowak, Robbins *et al.*, 2013), therefore it is very hard to render glass particles fully hydrophobic.

2.4. Measurement instrumentation

To observe the attachment of a solid particle on a gas bubble surface the in-house optical micro-bubble sensor (Ren, Wu *et al.*, 2011) developed at the Helmholtz Zentrum Dresden-Rossendorf was put to use in the present study. The sensor consists of two tubular waterproof housings facing each other's extremities. The gas bubble was placed between the two tubular shafts partly immersed in water. A distance of about 40 mm, which corresponded to about 25 bubble diameters, separated the two shafts. The first housing enclosed the CCD camera and the second enclosed the LED illumination system. The light source flashed in synchronisation with the camera exposure. A focus length of 20 mm allowed for a field of view of about 3.5x2.6 mm^2, which was large enough to hold the gas bubble and capture the entire particle attachment. Each image had a resolution of 640 x 480 pixels. With a particle terminal velocity ranging from $u_\infty = 1.5$ mm/s to $u_\infty = 7$ mm/s (See annex 1) and a frame rate of 120 images per second it resulted in a local particle displacement between two consecutive illumination pulses ranging from 10 µm to 60 µm.

2.5. Experimental data processing

The footage of a particle attachment was a very tedious task. The particle had to evolve over the course of the entire attachment process in the focus plane of the micro-bubble sensor. The attachment of a fibre was an even unlikelier event since the major axis also had to remain in the plane of focus so that the particle orientation could be determined. The chance of capturing the attachment of a very single particle was actually low. The facility did not allow the release of one particle at a time. Therefore only the head of the falling cloud, which had a local dilution greater than that of the bulk of the cloud, was here of interest. The reason behind the footage of the cloud head was twofold: 1. the chance of capturing single attachment in the field of view was increased and 2. the particle-induced flow and the inter-particle collisions near the gas bubble, which were observed to affect the attachment, could be avoided. While it was difficult to accurately estimate

the occurrence of an exploitable attachment, we found out that about 50 experimental test runs resulted in one exploitable attachment. A measurement campaign lasting several weeks was therefore necessary to capture the 30 attachments of elongated particles and the 4 attachments of spherical particles presented in the present work. Each successful capture of a particle attachment, in which the particle evolved in the focus plane, was exported in the form of an image sequence to the post-processing program Fiji. The image processing program is an open-source platform normally used for biological-image analysis (Schindelin, Arganda-Carreras *et al.*, 2012). After the threshold of each image sequence, a circle was fit to the gas bubble and polar coordinate system was defined. The diameter of the needle, which was of course known beforehand, was used as the reference length. During the approach the orientation of the major particle axis and its velocity could be automatically detected by fitting a two-dimensional ellipsoid. However during the sliding the particle shape could no longer be automatically discriminated from the gas bubble shadow. For this reason the determination of the major axis and the velocities were done manually for various images. It resulted in a time-consuming image processing.

2.6. Spherical particle transport model

The present experimental investigation was carried with “clean” bubbles, i.e. the gas-liquid interface underwent no contamination by frothers, which were previously found to significantly influence the collision efficiency (Sarrot, Guiraud *et al.*, 2005). Further information on the effect of partial and full interface contamination on the collision efficiency can be found in the study of Legendre, Sarrot *et al.* (2009). The physico-chemical interfacial forces normally prevail over the hydrodynamic forces only within a very short distance from the gas-liquid interface, typically for a gap value lower than $h < 0.1$ µm (Huang, Legendre *et al.*, 2012): a distance by several order of magnitude smaller than the particle size. Since the physic-chemical interfacial forces have little effect on the collision they were here left out. The history force and the lift force are of second order and can also be neglected (Nguyen, 2003). The effect of the Basset force even though it was included in the Lagrangian particle model of Verrelli, Koh *et al.* (2011) is often left out in other numerical studies (Nguyen and Nguyen, 2009). Thus retaining only the hydrodynamic drag exerted by the liquid phase, the gravity and the buoyancy, the vectorial transport equation of a point-like solid spherical particle evolving in the liquid phase therefore reads

$$m\frac{d\vec{u}}{dt} = -3\pi\mu d_p\,\vec{u} + \left(m - m_f\right)\vec{g}. \tag{6}$$

In the above equation $\vec{u}$ is the particle velocity vector. Since the stationary bubble is immersed in stagnant water the velocity of the liquid phase is set to zero throughout the simulation. The term m corresponds to the particle mass and m_f to the mass of liquid displaced by the particle. The term μ corresponds to the dynamic viscosity of the liquid phase. The transport equation can conveniently be expressed in terms of the two polar coordinates (r, ϕ), in which r is the distance from the bubble centre to the particle centre and ϕ the angle measured from the vertical axis (see Figure 3). The polar axis $\phi = 0$ coincides with the upstream pole of the gas bubble. Using the terminal velocity u_∞ defined in Eq. (1) the polar transformation of Eq. (6) leads to the following system of scalar equations

$$\frac{du_r}{dt} = -\left[\frac{(1+k_s)f_r}{\tau}\right]u_r + \left[\frac{u_\phi^2}{r} - \frac{u_\infty}{\tau}cos(\phi)\right], \tag{7}$$

$$\frac{du_\phi}{dt} = -\left[\frac{f_\phi}{\tau} + \frac{u_r}{r}\right]u_\phi + \left[\frac{u_\infty}{\tau}\sin(\phi)\right]. \tag{8}$$

The radial and tangential velocities are given by

$$u_r = \frac{dr}{dt} \quad , \quad u_\phi = r\frac{d\phi}{dt}. \tag{9}$$

The particle will deviate from its original trajectory as it approaches the bubble surface. To account for the change in the particle motion towards the bubble side the hydrodynamic force requires an artificial correction. Since the particle size is much smaller than the bubble size, it can be assumed that the particle encounters a fairly flat gas-liquid interface (Nguyen and Jameson, 2005). The radial and tangential drag components are therefore corrected using the following polynomial approximations (Huang, Legendre *et al.*, 2012)

$$f_r = 1 + \frac{3}{2}\lambda + \frac{9}{4}\lambda^2 + \frac{19}{8}\lambda^3 + \frac{93}{16}\lambda^4 + \frac{387}{32}\lambda^5 + \frac{1197}{64}\lambda^6 + \frac{5331}{128}\lambda^7 + \frac{19821}{256}\lambda^8 + \frac{76115}{512}\lambda^9 + \frac{3}{10}\left[\frac{(2\lambda)^{10}}{1+2\lambda}\right], \tag{10}$$

$$f_\phi = 1 - \frac{3}{4}\lambda + \frac{9}{16}\lambda^2 - \frac{59}{64}\lambda^3 + \frac{465}{256}\lambda^4 - \frac{15813}{7168}\lambda^5 + 2\left(\frac{\lambda^6}{1+\lambda}\right), \tag{11}$$

where the dimensionless variable λ equals $\lambda = 0.5d_p/(2h + d_p)$. The gap $h = r - 0.5(d_p + d_b)$ corresponds to smallest distance between the particle surface and the bubble surface. Close to the gas-bubble interface the particle typically experiences an increase in the hydrodynamic drag force

and a decrease in the tangential force. Far from the bubble the two approximations f_r and f_ϕ are smoothly brought back to unity using a blending function to exactly achieve the correct terminal velocity u_∞. The blending function is a smooth approximation of the Heaviside step function. It is here given by

$$H_V(h^*) = \frac{1}{2}\left(1 + \tanh\left[\frac{h^* - h_m^*}{\Delta h^*}\right]\right). \quad (12)$$

The upper script * indicates the normalisation of the gap with the reference scaling ($d_b/2$ for a length variable, see Eq. 14). With the smoothing centre $h_m^* = 0.6$ and the smoothing radius of $\Delta h^* = 0.3$ the final correction then takes the form $f_{r,\phi} = H_V + (1 - H_V) f_{r,\phi}$. The effect of the blending function can be seen in Figure 4. A cut off of the polynomial function to the 3rd order is also shown. The reduction of Eq. (10-11) to a third-order polynomial will largely affect the radial drag correction close to the gas-bubble interface, i.e. within $h^* < 0.1$. As in the original model of Huang, Legendre *et al.* (2012), the above 10th- and 6th-order polynomial approximations are here employed. Upon collision with the gas bubble the two drag correction factors no longer make sense and therefore they equal unity. The dimensionless friction factor k_s is introduced to correct the particle drag force during the sliding motion on the bubble surface. Wang, Zhou *et al.* (2003a) suggested, as is the case here, $k_s = 0.03$ for untreated glass beads interacting with with 'clean' bubbles. The value of k_s is however significantly affected by the use of collectors and frothers (Wang, Zhou *et al.*, 2003b). Methylated glass spheres showed an increase in the friction factor to $k_s = 0.1$. A gas bubble stabilised with sodium palmitic acid caused an increase in the friction factor to $k_s = 1$. The friction coefficient therefore needs particular attention since its value spans up to three orders of magnitude. During the approach the friction factor k_s is set to zero and the hydrodynamic drag force simply reduces to its well-known Stokes' formulation in the far-bubble region. During the sliding, which begins when the gap h drops to zero, the particle is in equilibrium in the radial direction. It means that the capillary adhesion force, the centrifugal force and the radial component of the gravity cancel one another out and $u_r = 0$. An extensive analysis on the adhesion forces can be found in the discussion. An implicit Euler backward scheme is used for the numerical integration of the two transport equations (Eq. 7-8) and a standard second-order Adams-Bashforth scheme is applied to compute the particle displacement (Eq. 9). These two integration schemes were previously found

appropriate to accurately compute the transport and the deposition of micron-sized particles (Lecrivain and Hampel, 2012, Lecrivain, Barry *et al.*, 2014).

3. Results and Discussions

3.1. Model validation

The performance of the transport model for spherical particles is initially compared with four experimental reference runs, which all involved the glass beads of spherical shape. The four experimental tests were carefully selected so that the corresponding collision angle ϕ_c of each run lied in one of the four collision intervals $I_{i=1..4}$

$$\begin{array}{ll} I_1: & \phi_c < 10° \\ I_2: & 10° \leq \phi_c < 30° \\ I_3: & 30° \leq \phi_c < 50° \\ I_4: & \phi_c \geq 50° \end{array} \tag{13}$$

Figure 5 presents the theoretical particle trajectories coloured by velocity magnitude with their experimental counterparts. At the initial simulation time $t = 0$ s the particle velocity equals the terminal velocity calculated from Eq. (1) and the horizontal particle position $R(t = 0) = R_\infty$ equals that measured from the very first occurrence of the particle in the camera field of view. The distance R corresponds to the shortest distance from the particle centre to the vertical rotation axis of the bubble ($x = 0$). All lengths and velocity variables are henceforth made non-dimensional with the bubble radius and with the terminal velocity so that, irrespective of the changes in the bubble and particle sizes, all data can easily be compared with one another. The distance R, for instance, is normalised as follows

$$R^* = \frac{2R}{d_b}, \tag{14}$$

and the instantaneous particle velocity is normalised as follows

$$u^* = \frac{|\vec{u}|}{u_\infty}. \tag{15}$$

The terminal velocity is experimentally calculated from the two furthest upstream particle positions. It can be seen that the theoretical particle trajectories and the theoretical particle velocities agree qualitatively well with the experimental results. Because of the increase in the drag force and the decrease in the tangential force that the particle encounters during its approach near the gas-bubble interface the particle smoothly moves away from the vertical rotation axis of

the bubble. The deviation of the particle trajectories can quantitatively be assessed with the collision angle ϕ_c. Using identical boundary conditions (d_p, d_b) and initial release conditions (u^*, R^*) it is found that the theoretical collision angles match remarkably well the experimental data in the three intervals $I_{i=1..3}$. The model however overestimates the deviation in the particle trajectory by about 15% for large collision angles. The reason behind the larger errors in the fourth interval I_4 is given in the next section 3.2.

3.2. Approach of the elongated particles

The velocity magnitude of each falling elongated particle during the approach phase is compared with that obtained from the four experimental runs involving the spherical particles and that obtained from the theoretical model. Figure 6 shows the velocity magnitude as a function of the polar coordinate r^*. Similarly to the model validation against the spherical glass bead data the results are sorted by collision angle and placed in one of the four collision intervals $I_{i=1..4}$ (Eq. 9). In each of the four subdiagrams the abscissa r^* decreases to unity. This lower bound indicates a collision with the gas bubble surface. The results show that the velocity magnitude of the approaching particles is not significantly affected by the particle aspect ratio. It is a major finding since even a model for spherical particles can be employed to predict the translational velocities and the trajectories of elongated particles. In the far-bubble region, found to be the region in which the normalised polar radius is greater than $r^* > 1.8$, the bubble has little effect on the particle motion: each particle descends with a constant velocity equalled to the terminal velocity u_∞. In the bubble region ($r^* < 1.8$) and for a collision angle lower than $\phi_c < 50°$ the velocity magnitude rapidly decreases. The closer the collision near the upstream pole the greater the deceleration. Upon collision with an angle lower than $\phi_c < 10°$ the particle experiences a loss in velocity of about 80% (interval I_1). In the third interval I_3 the particle experiences a loss in velocity of about 40%. As previously observed in the validation of the particle trajectories (Figure 5) the model exhibits an unrealistic behaviour for large collision angles (interval I_4). In the fourth interval I_4 the theoretically determined velocity magnitude increases as the particle approaches the bubble surface. Further analysis of the simulation data showed a strong decrease in the tangential drag force component, which in-turn caused this unnatural increase in the particle velocity magnitude. It seems that, for large collision angles, the two drag corrections (Eq. 10-11) lose validity when the particle comes very close to the gas-bubble interface, i.e. within $r^* < 1.1$.

3.3. Sliding of the elongated particles

The velocity magnitude was also measured during the sliding phase. As illustrated in Figure 7, it can be seen that the particle elongation does not influence the velocity magnitude in each collision interval. The model also performs remarkably well. The velocity magnitude reaches its maximum when the polar angle reaches 100°. The orientation of the particle major axis with the radial direction is denoted by the angle γ (See Figure 3 for an illustrative schematic). Figure 8 illustrates the two types of ellipsoidal attachments: the "weak attachment" and the "strong attachment". The weak attachment indicates a radial alignment of the fibre at the gas-liquid interface. Only one of the two fibre extremities eventually adheres to the gas-liquid interface ($\gamma = 0$ towards the end of the sliding). The strong attachment indicates a larger three-phase contact area. Throughout the sliding phase the particle major axis aligns with the gas-liquid interface ($\gamma = 90°$) which results in a tangential alignment of the fibre at the gas liquid interface. The evolution of the major axis orientation as a function of the polar angle over the course of the sliding is shown in Figure 9. The figure is divided into two subfigures. The subfigure (9a) on the left hand side encompasses the elongated particles for which a weak attachment was observed. The subfigure (9b) on the right hand side encompasses the elongated particles for which a strong attachment was observed. As expected the strong attachment involves a particle orientation which equals 90° throughout the entire attachment. During a weak attachment the elongated particle initially aligns with the bubble surface (tangential contact, $\gamma = 90°$) and when the polar angle reaches the surface bubble region $90° < \phi < 120°$ the particle orientation suddenly changes: the contact becomes radial ($\gamma = 0°$). Last but not least, about 90% of experimental runs, in which the collision angle exceeded the threshold $\phi_c > 30°$, resulted in a weak attachment (left subfigure 9a). Should the collision angle be lower than this threshold collision angle (grey area in the right subfigure 9b), the attachment was found take a strong form. The effect of the collision angle has a major effect on the fibre orientation during the sliding motion.

3.4. Discussions

3.4.1. Sliding time

The weak attachment is very likely due to the shorter time of "induction" (Yoon and Luttrell, 1989) which does not allow for the formation of a stronger tangential three-phase contact. Verrelli, Koh *et al.* (2012) experimentally measured the induction time of methylated borosilicate

glass spheres. The team showed that the induction time increased with the collision angle, i.e. a larger collision angle resulted in a longer time required for the film rupture to occur. For collision angles greater than $\phi_c > 30°$ the team estimated an induction time ranging from 0.1 to 0.2 s. A collision near the upstream pole resulted in a lower induction time of about 0.02 s. During a weak attachment and irrespective of its shape, it was here found that a particle colliding with the bubble at a polar angle greater than $\phi_c > 30°$ required on average 0.15 s to 0.2 s to reach the bubble equator, after which the particle changed its orientation γ. The present sliding time needed to reach the bubble equator is of course determined for glass beads with a contact angle of $\theta = 60 - 70°$ and can therefore not be directly compared with the induction time of glass particles with a surface treatment. Yet it seems that the sliding time needed to reach the bubble equator should be large enough for a strong attachment to occur.

3.4.2. Forces at the gas-liquid interface

Findings from this work along with the experimental observations of Wang, Zhou *et al.* (2003b) have shown that the maximum value, for which the rotational velocity reaches its maxima, is not exactly found at 90°, but at a polar angle located between 90° and 110°. Surprisingly it fairly corresponds to the range, in which the particle suddenly changes its orientation γ over the course of a weak attachment (Figure 9). Could it be that the change in the particle orientation during a weak attachment is triggered by the centrifugal force? It is therefore of interest to work out which forces prevail during the sliding process. The magnitude of the various forces are here derived from the theoretical work of Nguyen (2003). He developed a force balance model, in which a spherical particle is at rest at the downstream pole of a bubble, i.e. at $\phi = 180°$. Four major static forces were identified: the capillary force F_{cap}, the buoyancy F_b, the pressure force F_p and the particle weight F_g. In the following each force is normalised with the surface tension σ and the capillary length $L = \sqrt{\sigma/(\rho_L g)}$. The mathematical formulations are also simplified as a result of the small particle-to-bubble diameter ratio. The dimensionless capillary force, which tends to pull the solid particle into the gas phase, equals the product of the gas-liquid surface tension with the length of the three-phase contact line. Its formulation reads

$$\frac{F_{cap}(\phi = 180°)}{2\pi\sigma L} = \frac{1}{2}\left(\frac{d_p}{L}\right)\sin\alpha\,\sin(\theta - \alpha). \tag{16}$$

For the exact definition of the angle α the reader is referred to the original work of Nguyen (2003). Typically the total adhesion force is maximum for $\alpha = 28°$. Should the centrifugal force be introduced in the original force balance model of Nguyen (2003), the value of α, for which the adhesion force is maximum, will change. The force balance model of Nutt (1960) could for instance be employed. It has also been shown that the for a fixed particle volume, a prolate spheroid attaches even more strongly to a gas-liquid interface because of the larger particle-interface area (Davies, Kruger *et al.*, 2014). An exact solution of the various forces acting on the particle at the gas-bubble interface is however irrelevant in the present discussion since we only seek to compare their respective orders of magnitude. The hydrostatic pressure force of the liquid phase above the contact area at the gas-liquid interface is given by

$$\frac{F_h(\phi = 180°)}{2\pi\sigma L} = \frac{1}{4}\left(\frac{d_p}{L}\right)^2\left(\frac{d_b}{2L} - \frac{2L}{d_b}\right)\sin^2\alpha. \tag{17}$$

The buoyancy force, which largely applies to the particle volume immersed in the liquid phase, is defined as

$$\frac{F_b(\phi = 180°)}{2\pi\sigma L} = \frac{1}{48}\left(\frac{d_p}{L}\right)^3(2 + 3\cos\alpha - \cos^3\alpha). \tag{18}$$

The particle weight is given by

$$\frac{F_g(\phi = 180°)}{2\pi\sigma L} = \frac{1}{12}\left(\frac{d_p}{L}\right)^3 S. \tag{19}$$

Using the theoretical formulation of the centrifugal force derived by Dai, Dukhin *et al.* (1998), it can be shown that its magnitude is proportional to $\sin^2\phi$, and therefore the centrifugal force reaches its theoretical maxima at the bubble equator $\phi = 90°$. Figure 7 shows that the maximal sliding velocity roughly equals the terminal velocity. With a typical terminal velocity $u_\infty = 3$ mm/s (Annex 1) and an average bubble diameter $d_b = 1.4$ mm, a fair estimate of the centrifugal force at the equator can be given by

$$\frac{F_c(\phi = 90°)}{2\pi\sigma L} = \frac{1}{48}\left(\frac{d_p}{L}\right)^3\left(\frac{2u_\infty^2}{g d_b}\right) \approx 10^{-3}\frac{1}{48}\left(\frac{d_p}{L}\right)^3. \tag{20}$$

For comparison purposes all the above forces were made function of the ratio of the particle diameter to the capillary length. With a capillary length of about $L = 2.7$ mm this ratio becomes very small, i.e. $d_p/L \ll 1$. The particle buoyancy (Eq. 18) and the particle weight (Eq. 19) are therefore two orders of magnitude smaller than the capillary force. The centrifugal force (Eq. 20) is by even more orders of magnitude smaller than the capillary force. It therefore seems fair to

neglect the effect of the centrifugal force on the change in the fibre orientation over the course of a weak attachment.

3.4.3. Terminal velocity of the elongated particles

In the present model it was assumed that the particles were spherical. However, the drag of an elongated particle does not necessarily equal that of an equivalent sphere. The terminal velocity $u_\infty^{\parallel}$ of an elongated particle, which has its major axis parallel to the direction of motion (particle in a vertical position), will differ from the terminal velocity $u_\infty^{\perp}$ of the exact same particle descending with its major axis normal to the relative particle motion (particle in a horizontal position). Therefore the two shape factors $\kappa_\parallel$ and $\kappa_\perp$, defined as the ratio of the terminal velocity of an elongated particle to that of an equivalent sphere of same volume and density (Kasper, Niida *et al.*, 1985) are normally introduced

$$\kappa_\parallel = \frac{u_\infty^{\parallel}}{u_\infty^{eq}} \quad , \quad \kappa_\perp = \frac{u_\infty^{\perp}}{u_\infty^{eq}}. \tag{21}$$

In the above formulation u_∞^{eq} corresponds to the terminal velocity of a sphere of equivalent volume. Exact, limiting and approximate solutions for the drag on spheroids at creeping flow conditions using the slender-body theory were derived by Oberbeck (1876). As is the case here, a creeping flow indicates that the Reynolds number based on the particle diameter and the liquid viscosity is lower than unity. One of the approximations (Loth, 2008), for which the aspect ratio of a needle-like ellipsoid (prolate) is greater than unity, can be found in Table 2. The shape factors are calculated for an aspect ratio of 3 and 6. The theoretical value is compared with the experimental data derived from the work of Kasper, Niida *et al.* (1985). For a particle aspect ratio of $e = 3$ one can expect a maximum difference in the terminal velocity of about 30% compared to that of an equivalent sphere. This difference will increase to about 60 % for a particle aspect ratio equalled to $e = 6$. The present model, which involves spherical particles, therefore underestimates the translational velocities. It is however not directly shown in the figures since the velocity variables were made non-dimensional with the terminal velocity. The experimental determination of the terminal velocity was taken from the first two occurrences of the particle in the camera field of view. It was shown here that the particle velocity is affected within $r^* < 1.8$. Figure 8 and the two videos available in the supplementary material show that some particles enter the field of view at an altitude of about $r^* \approx 1.5$. It is therefore likely that the terminal velocity does not always exactly correspond to the one, which would be observed at a higher

altitude. Unfortunately there is no better alternative for determining the exact terminal velocity of the elongated particles.

4. Conclusions

The present work looked at the attachment of solid elongated particles on the surface of a stationary gas bubble immersed in stagnant water. It was shown that the particle aspect ratio has no significant effect on the translational velocities of the particles. The far-bubble region, in which the velocity of the particle is not affected by the bubble, was found to be the region in which the normalised polar radius was greater than $r^* > 1.8$. The results matched very well those obtained numerically with spheres as long as the collision angle remained lower than $\phi_c < 50°$. For the first time the existence of two types of attachment has been shown. Upon collision near the upstream pole of the gas bubble the major axis of the fibre aligns with the local bubble surface (tangential fibre alignment, strong attachment). If collision occurs at least 30° further downstream only head of the fibre is in contact with the gas-liquid interface (radial fibre alignment, weak attachment).

Acknowledgements

This work was supported by a Marie Curie International Outgoing Fellowship with the European Union Seventh Framework Program for Research and Technological Development (2007-2013) under the grant agreement number 623518.

References

Ahmed, N. and Jameson, G. J., 1985. The effect of bubble-size on the rate of flotation of fine particles. International Journal of Mineral Processing 14, 195-215.

Albijanic, B., Ozdemir, O., Nguyen, A. V. and Bradshaw, D., 2010. A review of induction and attachment times of wetting thin films between air bubbles and particles and its relevance in the separation of particles by flotation. Advances in Colloid and Interface Science 159, 1-21.

Brunauer, S., Emmett, P. H. and Teller, E., 1938. Adsorption of gases in multimolecular layers. Journal of the American Chemical Society 60, 309-319.

Cho, Y. S. and Laskowski, J. S., 2002. Effect of flotation frothers on bubble size and foam stability. International Journal of Mineral Processing 64, 69-80.

513 Crowe, C. T., Schwarzkopf, J. D., Sommerfeld, M. and Tsuji, Y., 2011. Multiphase flows with
514 droplets and particles, second edition. CRC Press.
515 Dai, Z., Dukhin, S., Fornasiero, D. and Ralston, J., 1998. The inertial hydrodynamic interaction
516 of particles and rising bubbles with mobile surfaces. J Colloid Interface Sci 197, 275-292.
517 Das, S. C., Larson, I., Morton, D. A. and Stewart, P. J., 2011. Determination of the polar and total
518 surface energy distributions of particulates by inverse gas chromatography. Langmuir 27, 521-
519 523.
520 Davies, G. B., Kruger, T., Coveney, P. V. and Harting, J., 2014. Detachment energies of
521 spheroidal particles from fluid-fluid interfaces. J Chem Phys 141, 154902.
522 Forssberg, K. S. E., Subrahmanyam, T. V. and Nilsson, L. K., 1993. Influence of grinding
523 method on complex sulphide ore flotation: A pilot plant study. International Journal of
524 Mineral Processing 38, 157-175.
525 Fuerstenau, M. C., Jameson, G. J. and Yoon, R.-H., 2007. Froth flotation: A century of
526 innovation. Society for Mining, Metallurgy and Exploration, Inc. (SME).
527 Gamble, J. F., Leane, M., Olusanmi, D., Tobyn, M., Supuk, E., Khoo, J. and Naderi, M., 2012.
528 Surface energy analysis as a tool to probe the surface energy characteristics of micronized
529 materials-a comparison with inverse gas chromatography. International Journal of
530 Pharmaceutics 422, 238-244.
531 Gu, G., Sean Sanders, R., Nandakumar, K., Xu, Z. and Masliyah, J. H., 2004. A novel
532 experimental technique to study single bubble–bitumen attachment in flotation. International
533 Journal of Mineral Processing 74, 15-29.
534 Huang, Z., Legendre, D. and Guiraud, P., 2011. A new experimental method for determining
535 particle capture efficiency in flotation. Chemical Engineering Science 66, 982-997.
536 Huang, Z., Legendre, D. and Guiraud, P., 2012. Effect of interface contamination on particle-
537 bubble collision. Chemical Engineering Science 68, 1-18.
538 Hubička, M., Basařová, P. and Vejražka, J., 2013. Collision of a small rising bubble with a large
539 falling particle. International Journal of Mineral Processing 121, 21-30.
540 Jameson, G. J., 2010. Advances in fine and coarse particle flotation. Canadian Metallurgical
541 Quarterly 49, 325-330.
542 Kasper, G., Niida, T. and Yang, M., 1985. Measurements of viscous drag on cylinders and chains
543 of spheres with aspect ratios between 2 and 50. Journal of Aerosol Science 16, 535-556.

544 Kemper, M., 1999. State-of-the-art and new technologies in flotation deinking. International
545 Journal of Mineral Processing 56, 317-333.
546 Koh, P. T. L., Hao, F. P., Smith, L. K., Chau, T. T. and Bruckard, W. J., 2009. The effect of
547 particle shape and hydrophobicity in flotation. International Journal of Mineral Processing 93,
548 128-134.
549 Kursun, H. and Ulusoy, U., 2006. Influence of shape characteristics of talc mineral on the column
550 flotation behavior. International Journal of Mineral Processing 78, 262-268.
551 Lecrivain, G., Barry, L. and Hampel, U., 2014. Three-dimensional simulation of multilayer
552 particle deposition in an obstructed channel flow. Powder Technology 258, 134-143.
553 Lecrivain, G. and Hampel, U., 2012. Influence of the lagrangian integral time scale estimation in
554 the near wall region on particle deposition. ASME Journal of Fluids Engineering 134, 1-6.
555 Legendre, D., Sarrot, V. and Guiraud, P., 2009. On the particle inertia-free collision with a
556 partially contaminated spherical bubble. International Journal of Multiphase Flow 35, 163-
557 170.
558 Loth, E., 2008. Drag of non-spherical solid particles of regular and irregular shape. Powder
559 Technology 182, 342-353.
560 Mohammadi-Jam, S. and Waters, K. E., 2014. Inverse gas chromatography applications: A
561 review. Adv Colloid Interface Sci 212, 21-44.
562 Nguyen, A. V., 2003. New method and equations for determining attachment tenacity and
563 particle size limit in flotation. International Journal of Mineral Processing 68, 167-182.
564 Nguyen, A. V. and Jameson, G. J., 2005. Sliding of fine particles on the slip surface of rising gas
565 bubbles: Resistance of liquid shear flows. International Journal of Multiphase Flow 31, 492-
566 513.
567 Nguyen, P. T. and Nguyen, A. V., 2009. Validation of the generalised sutherland equation for
568 bubble–particle encounter efficiency in flotation: Effect of particle density. Minerals
569 Engineering 22, 176-181.
570 Nowak, E., Robbins, P., Combes, G., Stitt, E. H. and Pacek, A. W., 2013. Measurements of
571 contact angle between fine, non-porous particles with varying hydrophobicity and water and
572 non-polar liquids of different viscosities. Powder Technology 250, 21-32.
573 Nutt, C. W., 1960. Froth flotation - the adhesion of solid particles to flat interfaces and bubbles.
574 Chemical Engineering Science 12, 133-141.

575 Oberbeck, A., 1876. Über stationäre flüssigkeitsbewegungen mit berücksichtigung der inneren
576 reibung. Journal für die reine und angewandte Mathematik 81, 62-81.
577 Rahimi, M., Dehghani, F., Rezai, B. and Aslani, M. R., 2012. Influence of the roughness and
578 shape of quartz particles on their flotation kinetics. International Journal of Minerals
579 Metallurgy and Materials 19, 284-289.
580 Ralston, J., Fornasiero, D. and Hayes, R., 1999. Bubble–particle attachment and detachment in
581 flotation. International Journal of Mineral Processing 56, 133-164.
582 Ren, Y., Wu, Z., Ondruschka, B., Braeutigam, P., Franke, M., Nehring, H. and Hampel, U., 2011.
583 Oxidation of phenol by microbubble-assisted microelectrolysis. Chemical Engineering &
584 Technology 34, 699-706.
585 Rosenqvist, T., 2004. Principles of extractive metallurgy. Tapir Academic Press.
586 Rubio, J., Souza, M. L. and Smith, R. W., 2002. Overview of flotation as a wastewater treatment
587 technique. Minerals Engineering 15, 139-155.
588 Sarrot, V., Guiraud, P. and Legendre, D., 2005. Determination of the collision frequency between
589 bubbles and particles in flotation. Chemical Engineering Science 60, 6107-6117.
590 Schindelin, J., Arganda-Carreras, I., Frise, E., Kaynig, V., Longair, M., Pietzsch, T., Preibisch,
591 S., Rueden, C., Saalfeld, S., Schmid, B., Tinevez, J.-Y., White, D. J., Hartenstein, V., Eliceiri,
592 K., Tomancak, P. and Cardona, A., 2012. Fiji: An open-source platform for biological-image
593 analysis. Nature Methods 9, 676-682.
594 Schulze, H. J., 1989. Hydrodynamics of bubble-mineral particle collisions. Mineral Processing
595 and Extractive Metallurgy Review 5, 43-76.
596 Schulze, H. J., 1992. Probability of particle attachment on gas bubbles by sliding. Advances in
597 Colloid and Interface Science 40, 283-305.
598 Susana, L., Campaci, F. and Santomaso, A. C., 2012. Wettability of mineral and metallic
599 powders: Applicability and limitations of sessile drop method and washburn's technique.
600 Powder Technology 226, 68-77.
601 Tao, D., 2005. Role of bubble size in flotation of coarse and fine particles—a review. Separation
602 Science and Technology 39, 741-760.
603 Tino, E., Dieter, W., Lama, N. and Klaus, A., 1996. Dehydration of glass surfaces studied by
604 contact angle measurements. Journal of Colloid and Interface Science 179, 635-636.
605 van Oss, C. J., 2003. Long-range and short-range mechanisms of hydrophobic attraction and
606 hydrophilic repulsion in specific and aspecific interactions. J Mol Recognit 16, 177-190.

van Oss, C. J., Giese, R. F. and Docoslis, A., 2005. Hyperhydrophobicity of the water-air interface. Journal of Dispersion Science and Technology 26, 585-590.

VDI-GVC, 2013. Verein Deutscher Ingenieure (VDI) - Gesellschaft Verfahrenstechnik und Chemieingenieurwesen (GVC), Wärmeatlas, 11th Edition. VDI-Verlag, Springer.

Verrelli, D. I., Bruckard, W. J., Koh, P. T. L., Schwarz, M. P. and Follink, B., 2014. Particle shape effects in flotation. Part 1: Microscale experimental observations. Minerals Engineering 58, 80-89.

Verrelli, D. I., Koh, P. T. L., Bruckard, W. J. and Schwarz, M. P., 2012. Variations in the induction period for particle-bubble attachment. Minerals Engineering 36-38, 219-230.

Verrelli, D. I., Koh, P. T. L. and Nguyen, A. V., 2011. Particle–bubble interaction and attachment in flotation. Chemical Engineering Science 66, 5910-5921.

Wang, W., Zhou, Z., Nandakumar, K., Xu, Z. and Masliyah, J. H., 2003a. Attachment of individual particles to a stationary air bubble in model systems. International Journal of Mineral Processing 68, 47-69.

Wang, W., Zhou, Z., Nandakumar, K., Xu, Z. and Masliyah, J. H., 2003b. Effect of surface mobility on the particle sliding along a bubble or a solid sphere. Journal of Colloid and Interface Science 259, 81-88.

Ye, Y., Khandrika, S. M. and Miller, J. D., 1989. Induction-time measurements at a particle bed. International Journal of Mineral Processing 25, 221-240.

Yekeler, M., Ulusoy, U. and Hiçyılmaz, C., 2004. Effect of particle shape and roughness of talc mineral ground by different mills on the wettability and floatability. Powder Technology 140, 68-78.

Yoon, R. H. and Luttrell, G. H., 1989. The effect of bubble size on fine particle flotation. Mineral Processing and Extractive Metallurgy Review 5, 101-122.

Fig1

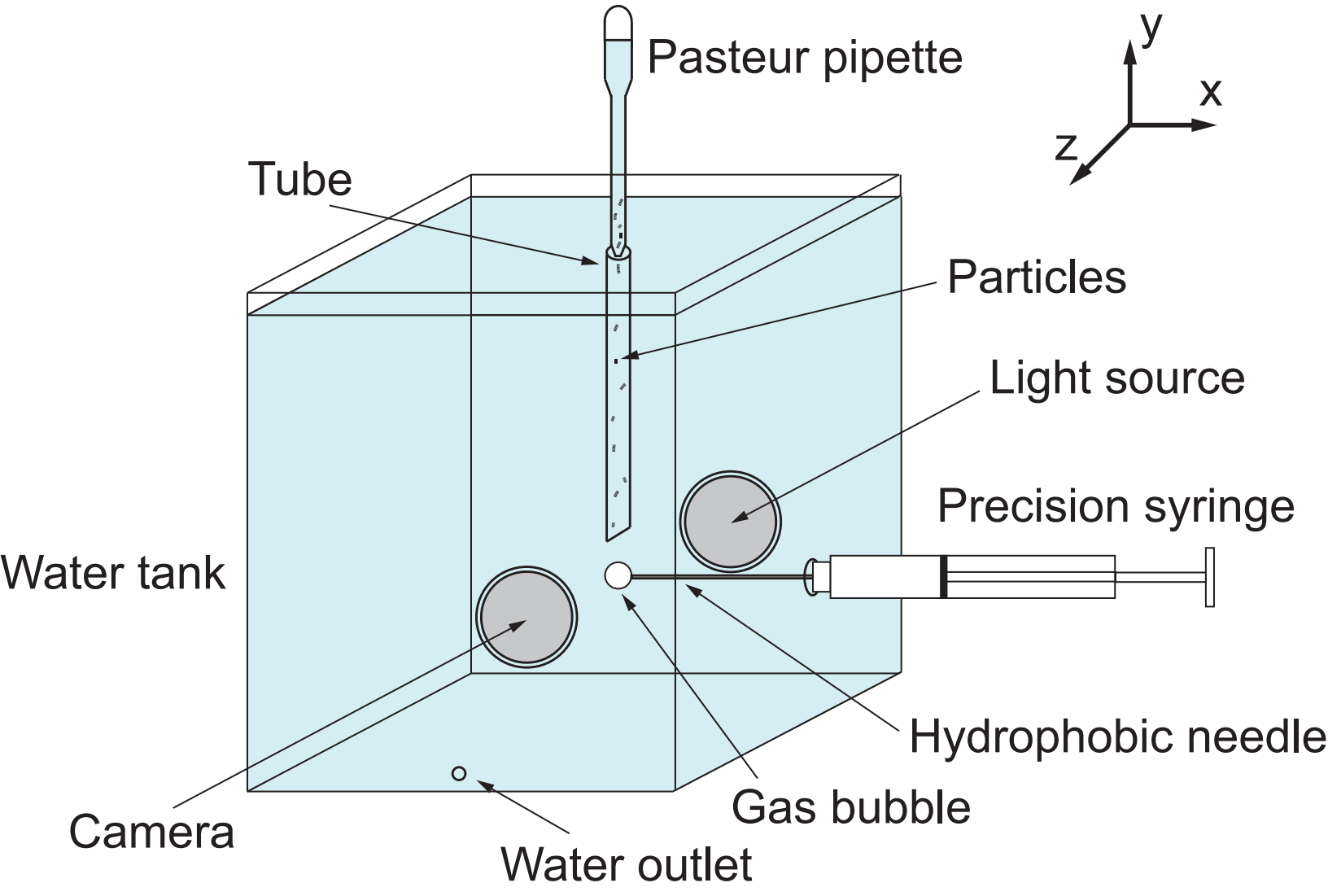
Pasteur pipette
y
x
z
Tube
Particles
Light source
Precision syringe
Water tank
Hydrophobic needle
Gas bubble
Camera
Water outlet

Fig2

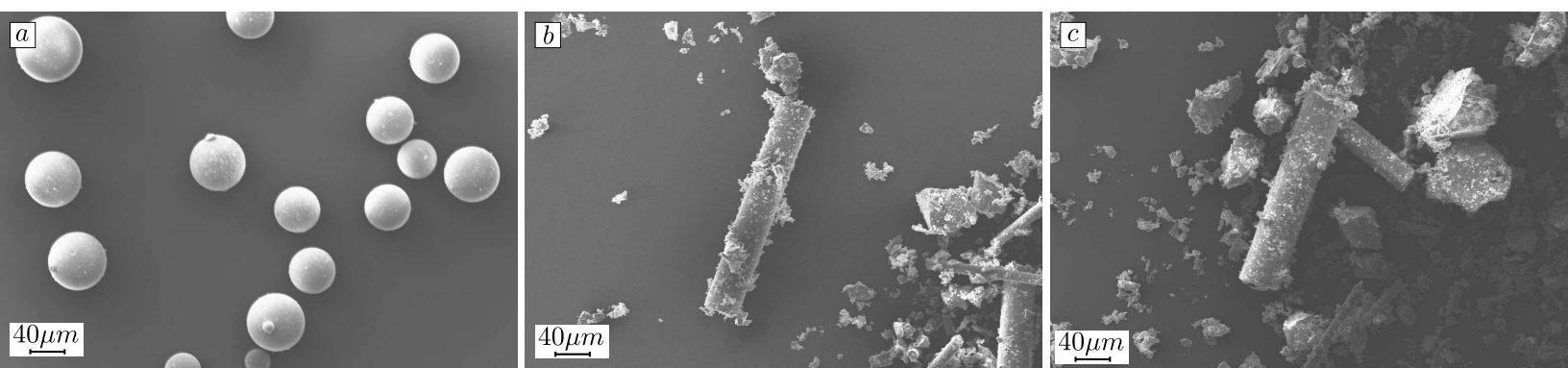

Fig3

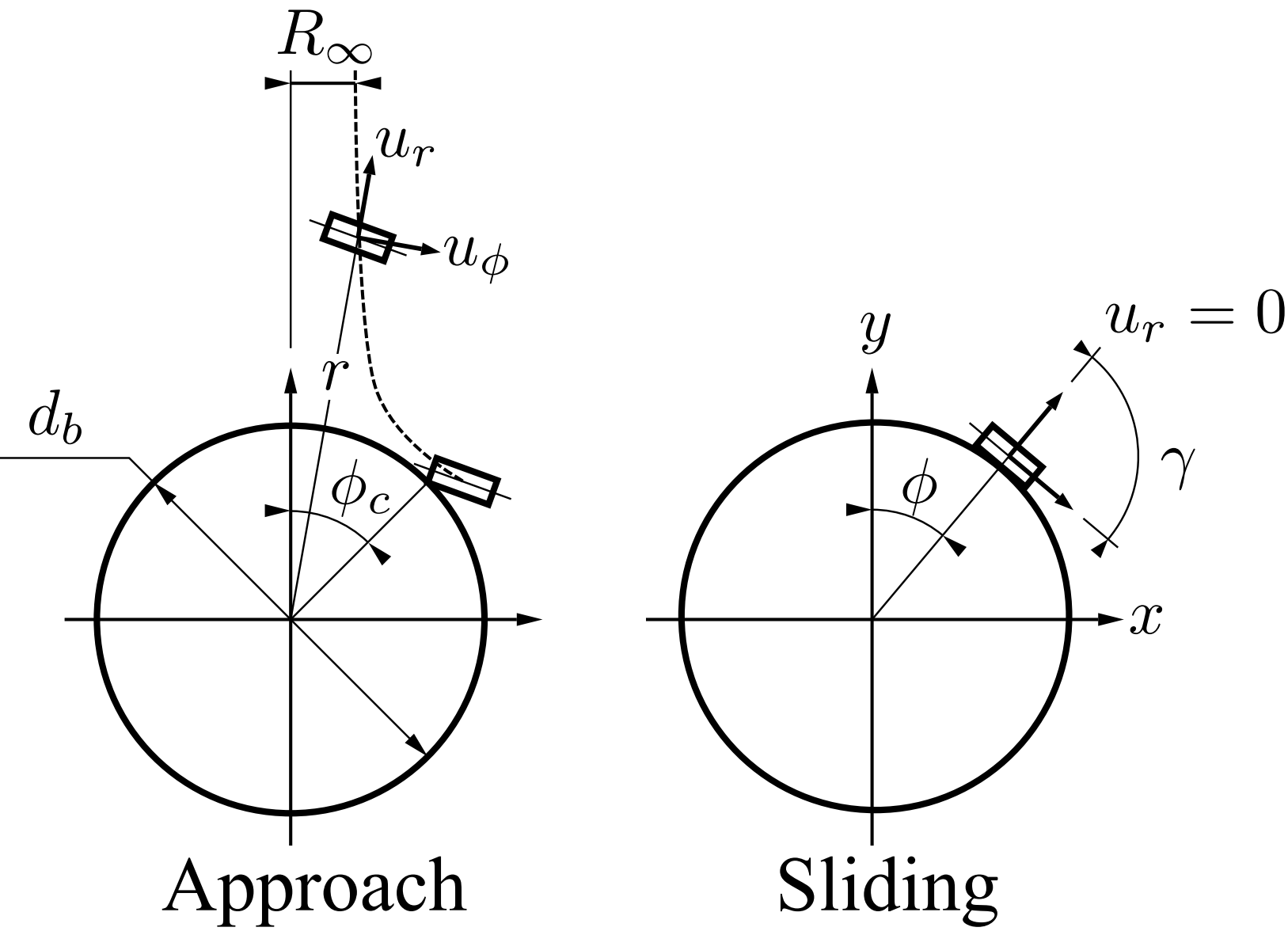

Fig4

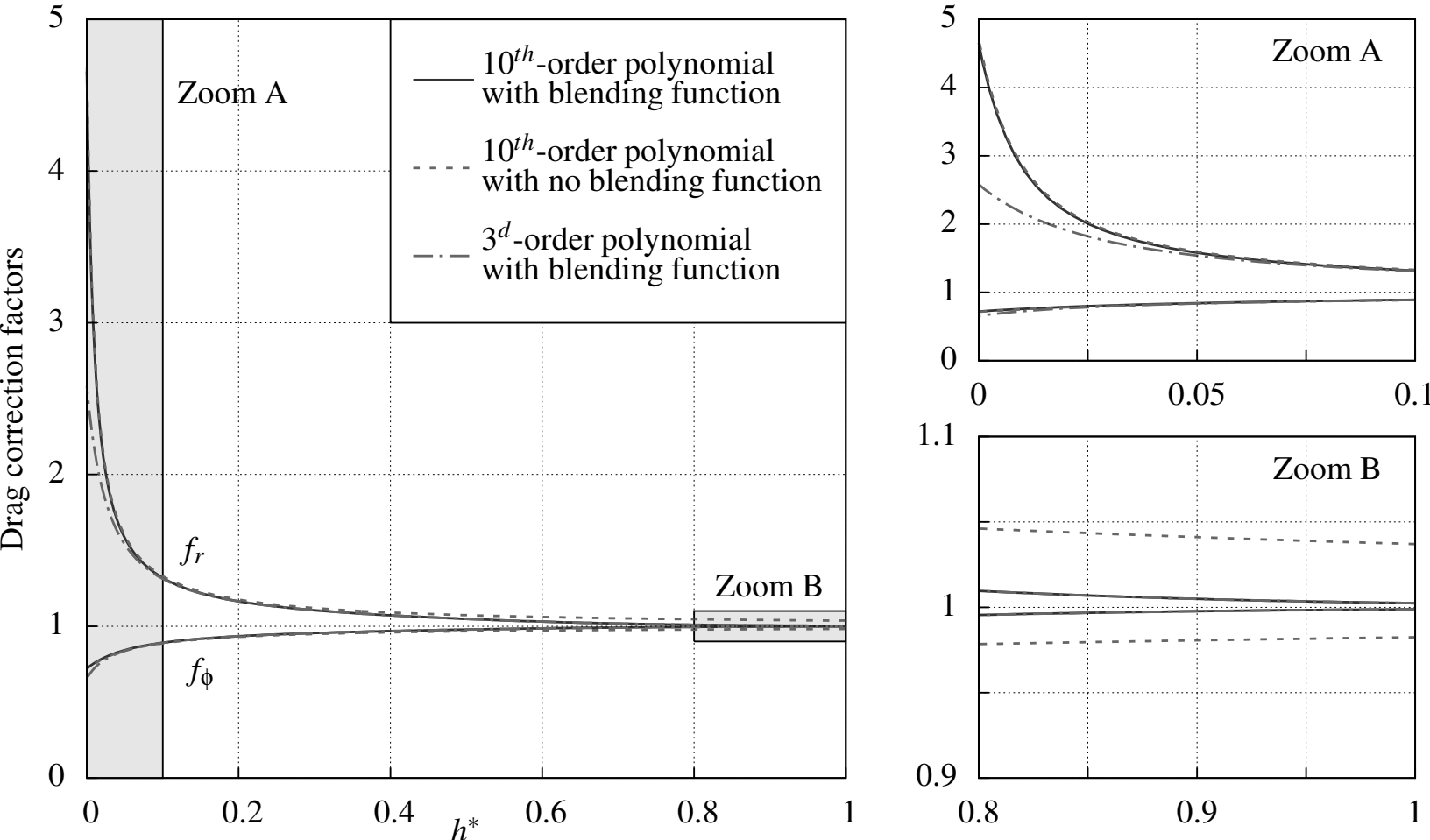
Zoom A
10^{th}-order polynomial with blending function
10^{th}-order polynomial with no blending function
3^{d}-order polynomial with blending function
Zoom B
f_r
f_ϕ
Drag correction factors
h^*
0
0.2
0.4
0.6
0.8
1
0
1
2
3
4
5
Zoom A
0
0.05
0.1
0
1
2
3
4
5
Zoom B
0.8
0.9
1
0.9
1
1.1

Fig5

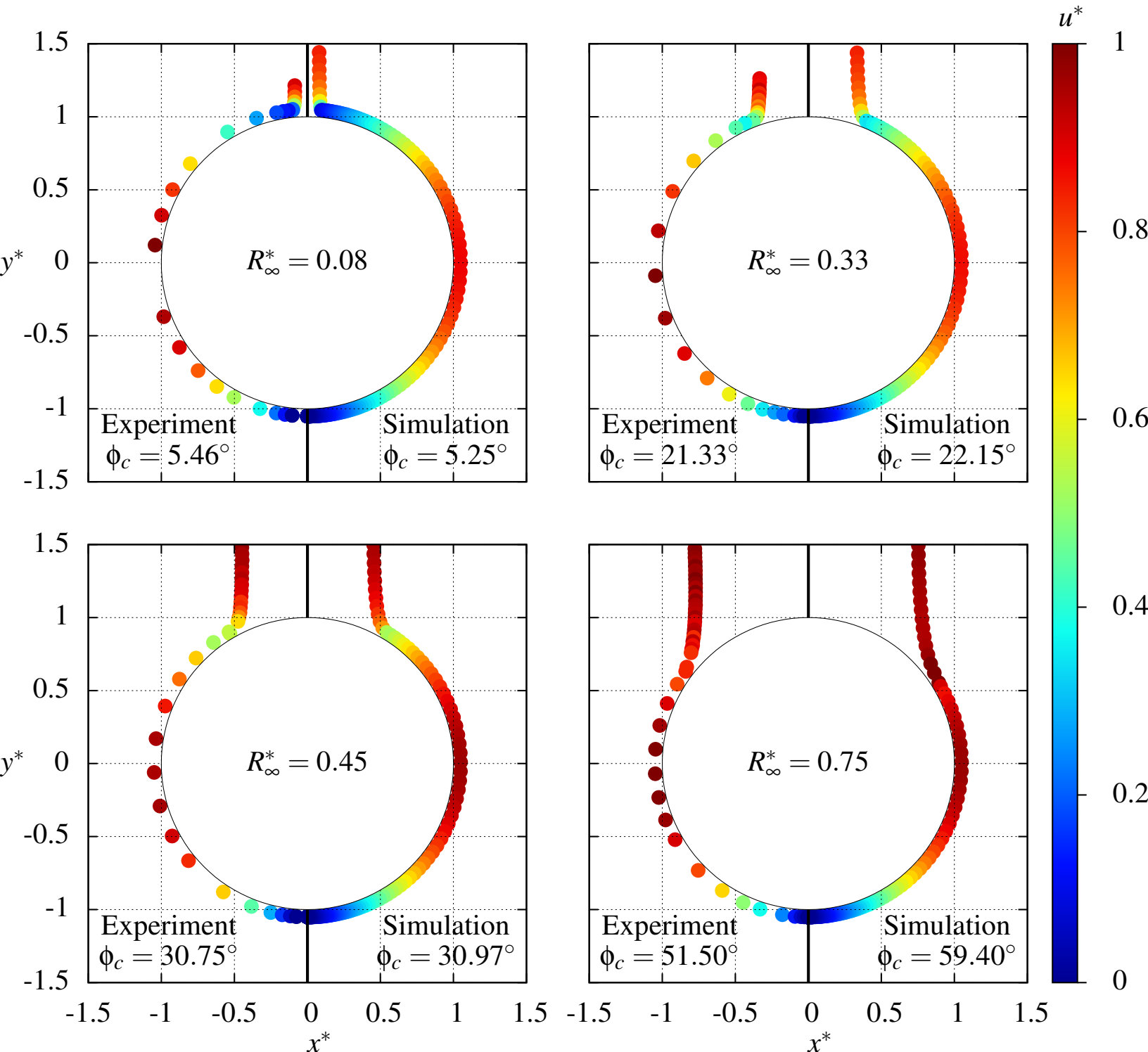
$R^*_\infty = 0.08$
Experiment
$\phi_c = 5.46°$
Simulation
$\phi_c = 5.25°$
$R^*_\infty = 0.33$
Experiment
$\phi_c = 21.33°$
Simulation
$\phi_c = 22.15°$
$R^*_\infty = 0.45$
Experiment
$\phi_c = 30.75°$
Simulation
$\phi_c = 30.97°$
$R^*_\infty = 0.75$
Experiment
$\phi_c = 51.50°$
Simulation
$\phi_c = 59.40°$
y^*
x^*
u^*
1.5
1
0.5
0
-0.5
-1
-1.5
0.8
0.6
0.4
0.2

Fig6

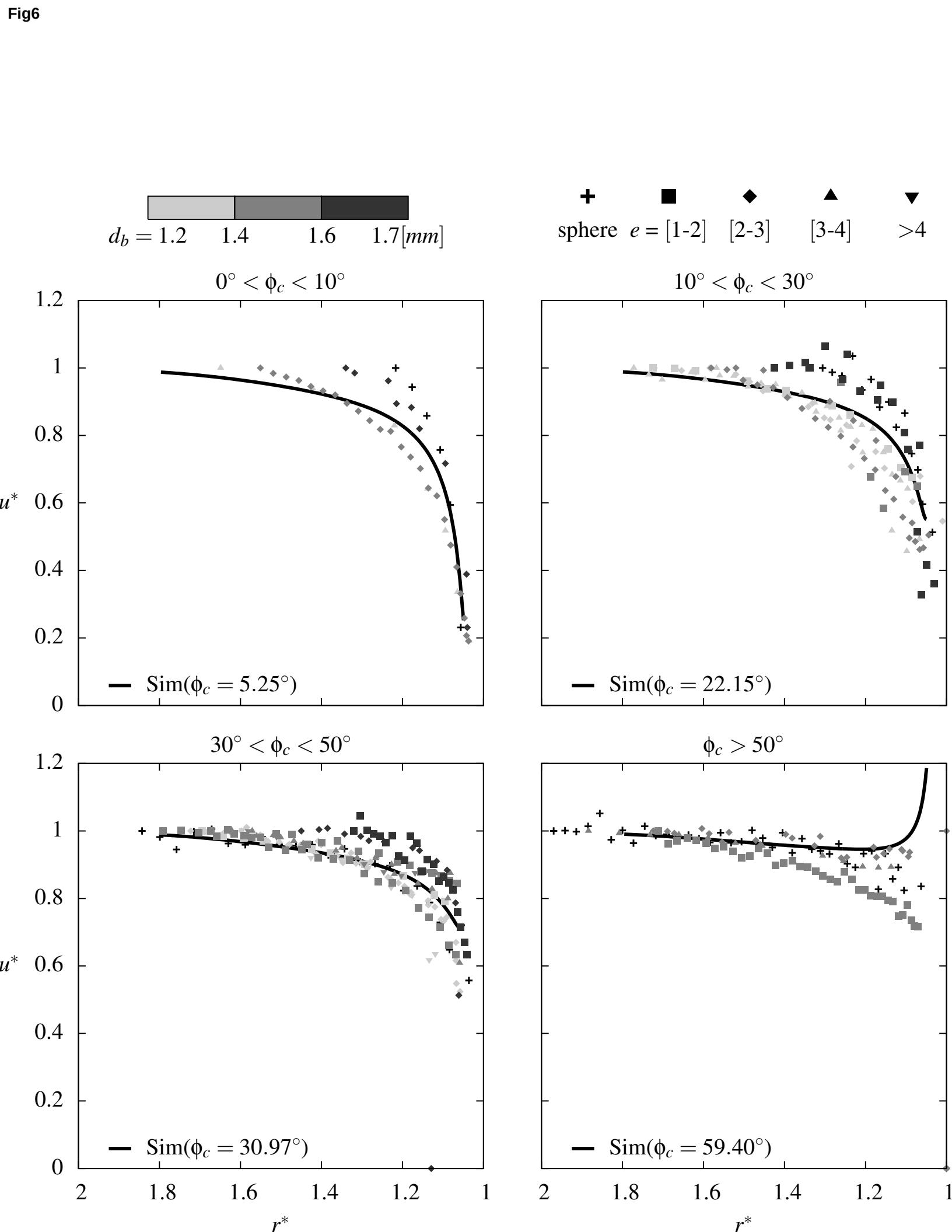
$d_b = 1.2$ 1.4 1.6 1.7[mm]
sphere e = [1-2] [2-3] [3-4] >4
$0° < \phi_c < 10°$
$10° < \phi_c < 30°$
$30° < \phi_c < 50°$
$\phi_c > 50°$
Sim($\phi_c = 5.25°$)
Sim($\phi_c = 22.15°$)
Sim($\phi_c = 30.97°$)
Sim($\phi_c = 59.40°$)
u^*
r^*
0
0.2
0.4
0.6
0.8
1
1.2
2
1.8
1.6
1.4
1.2
1

Fig7

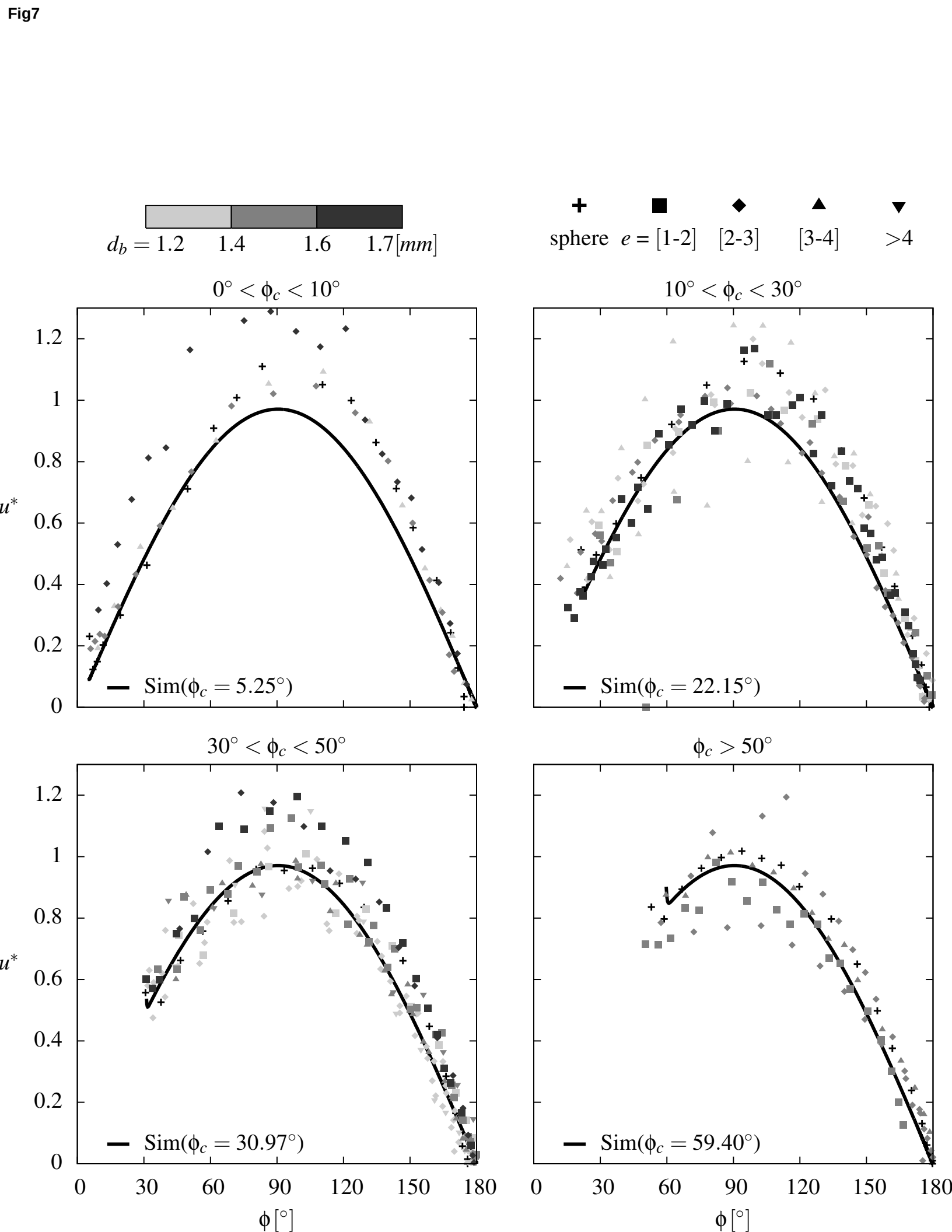
$d_b = 1.2$ 1.4 1.6 1.7[mm]
sphere e = [1-2] [2-3] [3-4] >4
$0° < \phi_c < 10°$
$10° < \phi_c < 30°$
$30° < \phi_c < 50°$
$\phi_c > 50°$
Sim($\phi_c = 5.25°$)
Sim($\phi_c = 22.15°$)
Sim($\phi_c = 30.97°$)
Sim($\phi_c = 59.40°$)
u^*
ϕ [°]
0 0.2 0.4 0.6 0.8 1 1.2
0 30 60 90 120 150 180

Fig8

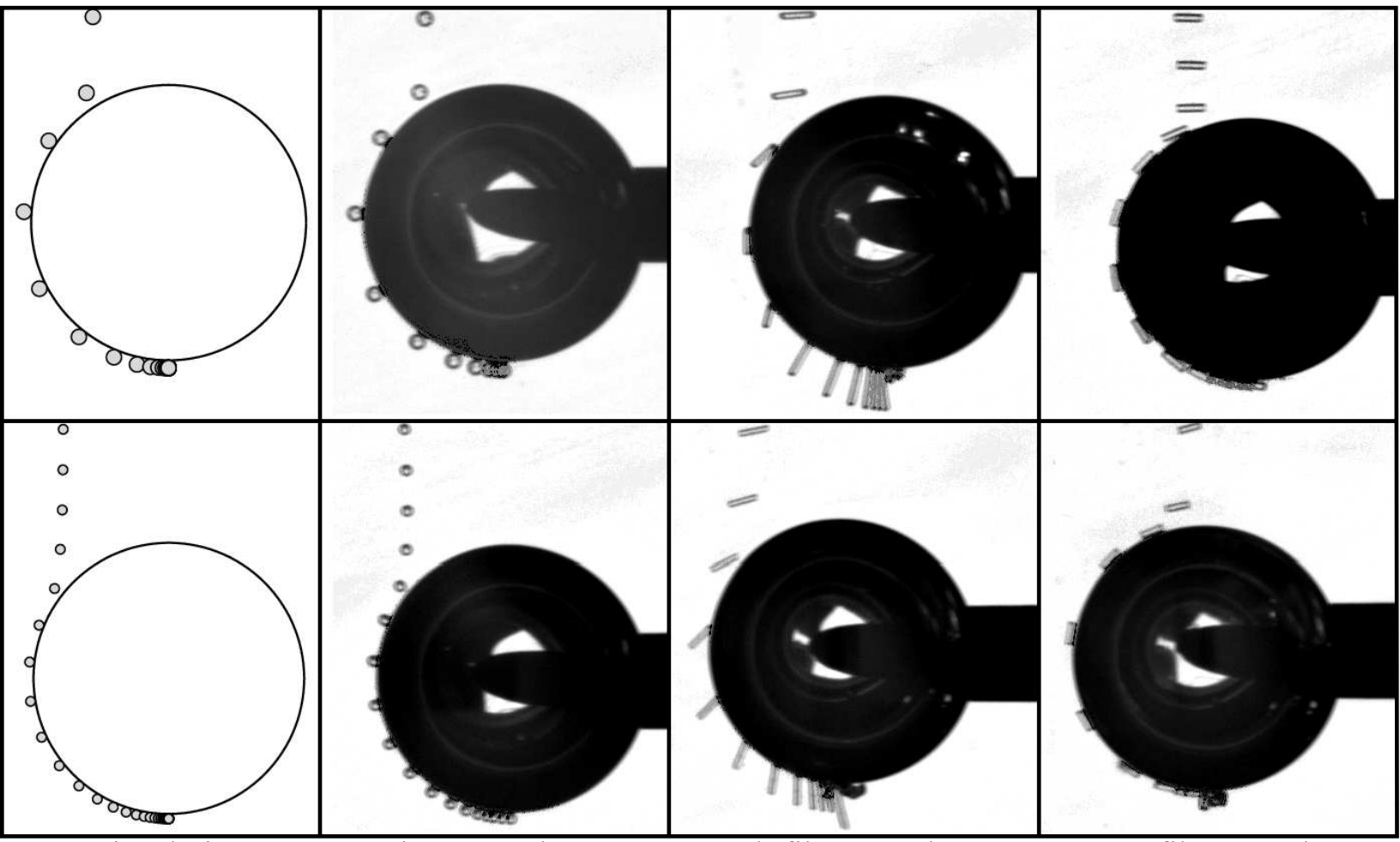
Simulation
Sphere attachment
Weak fibre attachment
Strong fibre attachment

Fig9

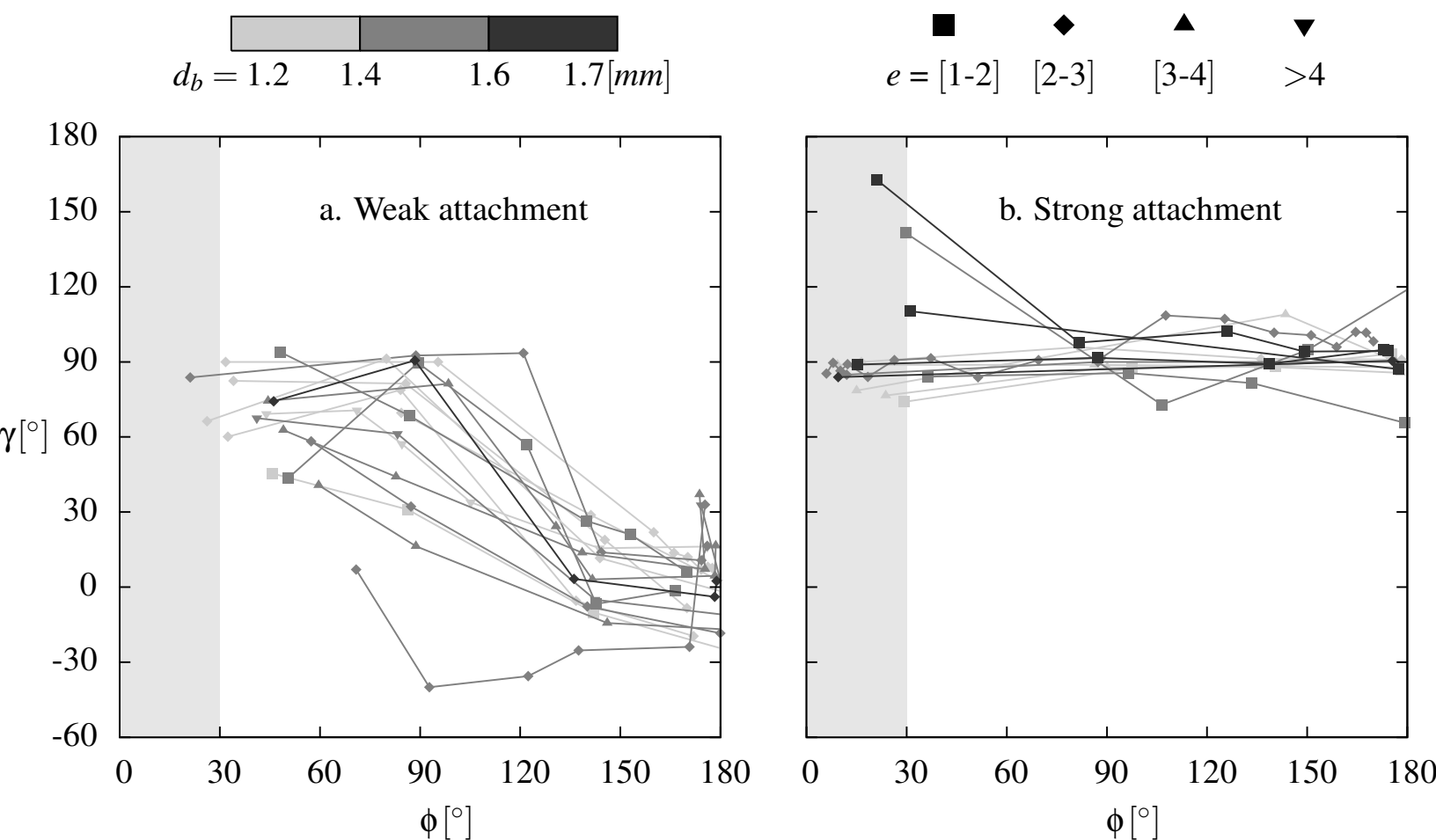
$d_b = 1.2$ 1.4 1.6 1.7[mm]
e = [1-2] [2-3] [3-4] >4
a. Weak attachment
b. Strong attachment
γ[°]
ϕ[°]
180
150
120
90
60
30
0
-30
-60
0 30 60 90 120 150 180

Tab1

material	S_m^{BET} [m^2/g]	surface coverage	γ^d [mJ/m^2]	γ^- [mJ/m^2]	γ^+ [mJ/m^2]	γ^+ [mJ/m^2]	ΔG_{pwb} [mJ/m^2]	θ [°]
Liquid water	-	-	18.0	21.1	21.1	60.2	-	-
Gas bubble	-	-	0.0	0.0	0.0	0.0	-	-
spherical particles	0.069	1 %	47.6 ±3.5	3.5 ±1.2	1.6 ±0.3	52.2 ±4.8	-33.3 ±9.0	63.5 ±6.7
		10 %	49.3 ±3.3	3.8 ±1.2	0.9 ±0.2	53.1 ±4.4	-34.0 ±8.8	64.2 ±6.3
		100 %	49.3 ±3.4	3.5 ±1.0	0.5 ±0.2	52.1 ±4.2	-36.8 ±8.7	67.2 ±5.8
elongated particles	0.470	1 %	37.4 ±0.3	4.6 ±0.1	4.0 ±0.0	46.0 ±0.4	-30.3 ±3.4	60.2 ±0.6
		10 %	40.8 ±0.6	3.3 ±0.2	1.0 ±0.1	44.5 ±0.8	-40.0 ±4.0	70.4 ±1.2
		100 %	40.8 ±0.9	3.0 ±0.2	1.1 ±0.1	44.4 ±1.1	-40.7 ±4.4	71.1 ±1.4

Tab2

	$\kappa_{\parallel}$	$\kappa_{\perp}$
Approximation $(1 < e < 6)$	$\left(\frac{4}{5}+\frac{e}{5}\right)e^{-1/3}$	$\left(\frac{3}{5}+\frac{2e}{5}\right)e^{-1/3}$
$e = 3$ (Approximation1)	0.97	1.25
$e = 3$ (Experiment2)	1.06	1.26
$e = 6$ (Approximation1)	1.10	1.65
$e = 6$ (Experiment2)	1.20	1.52

Figure captions:

Figure 1: Schematic of the test facility.

Figure 2: Images of the spherical (a) and elongated particles (b, c) obtained with scanning electron microscope.

Figure 3: Schematic representation of an elongated particle in its polar system during the approach and the sliding phase.

Figure 4: Radial and tangential drag correction factors shown as a function of the gap.

Figure 5: Validation of simulated trajectories coloured by velocity magnitude. Simulations and experiments were performed with spherical particles.

Figure 6: Evolution of the particle velocity magnitude during the approach phase. The data are sorted by collision angles.

Figure 7: Evolution of the particle velocity magnitude during the sliding phase. The data are sorted by collision angles.

Figure 8: Simulated attachment of a spherical particle, experimental attachment of a spherical particle, experimental weak attachment of an elongated particle and experimental strong attachment of an elongated particle (from left to right).

Figure 9: About 90% of experimental runs, in which the collision angle exceeded the threshold $\phi_c > 30°$, resulted in a weak attachment (Subfigure a). Should the collision angle be lower than this threshold collision angle (grey area in Subfigure b), the attachment takes a strong form.

Table captions:

Table 1: Measured hydrophobicity of the spherical particles and of the elongated particles at surface coverages of 1 %, 10 % and 100 %.

Table 2: Estimations of the two shape factors of an elongated particle. The approximation is derived from the work of Loth (2008). The experimental values are measured from a falling chain of beads (Kasper, Niida et al., 1985).

Annex1

Click here to download Electronic Annex: annex1.docx

	Particle ID	e	major axis length	u_∞	R_∞^*	ϕ_c	d_b
		[-]	[µm]	[mm/s]	[-]	[°]	[µm]
elongated particles (Experiment)	1	3.5	181	3.00	0.47	23.72	1363.1
	2	2.0	143	6.80	0.47	31.74	1378.2
	3	2.5	160	5.50	0.13	16.42	1378.2
	4	2.2	155	6.80	0.54	39.70	1372.8
	5	3.6	215	6.50	0.27	15.03	1378.2
	6	4.8	285	8.50	0.70	43.95	1378.2
	7	1.7	106	4.50	0.70	45.63	1316.7
	8	1.9	118	4.30	0.40	29.35	1306.3
	9	2.3	144	4.63	0.57	32.42	1345.0
	10	2.5	164	4.57	0.49	34.11	1345.0
	11	3.5	227	5.90	0.21	9.27	1265.5
	12	2.4	148	5.70	0.71	57.38	1430.1
	13	2.9	190	3.50	0.38	21.15	1430.1
	14	2.2	143	2.80	0.08	5.99	1430.1
	15	1.8	108	2.30	0.73	50.48	1418.9
	16	1.1	110	7.80	0.46	29.82	1409.2
	17	2.9	177	4.60	0.42	26.19	1384.5
	18	1.5	102	4.00	0.68	48.10	1458.5
	19	2.3	162	6.20	0.23	12.06	1483.0
	20	6.7	432	7.40	0.74	41.06	1455.1
	21	3.0	179	5.40	0.72	49.02	1450.2
	22	2.1	120	2.73	0.98	70.86	1463.0
	23	3.7	226	5.79	0.62	44.45	1408.9
	24	3.5	249	7.97	3.48	59.62	1525.3
	25	1.2	100	5.52	1.18	36.29	1525.3
	26	1.6	105	1.61	0.47	31.07	1666.9
	27	2.6	168	3.24	0.19	9.50	1671.6
	28	2.0	138	4.19	0.67	46.15	1626.2
	29	1.7	110	3.64	0.19	15.26	1690.9
	30	1.4	101	3.94	0.33	20.96	1690.9
spherical particles (Experiment)	1		122	4.36	0.08	5.46	1690.1
	2		95	2.58	0.33	21.33	1674.8
	3		108	3.94	0.45	30.75	1462.2
	4		95	2.54	0.75	51.50	1391.6
spherical particles (Simulation)	1		80	5.25	0.08	5.25	1600.0
	2		80	5.25	0.33	22.15	1600.0
	3		80	5.25	0.45	30.97	1600.0
	4		80	5.25	0.75	59.40	1600.0

Annex 1: Short summary of particle properties.

Video of a weak attchment

Click here to download Supplemental Multimedia File: weakAttachment.avi

Video of a strong attachment

Click here to download Supplemental Multimedia File: strongAttachment.avi